Lab on a Chip

PAPER

View Article Online
View Journal

Cite this: DOI: 10.1039/d6lc00047a

Acoustofluidic trapping of microparticles to axially centered wires in cylindrical microcapillaries

Ruben J. Trujillo,[a] Phung H. Bui,[a] Andrew P. Shreve,[a] Matthew J. Campen,†[b] Menake E. Piyasena†[c] and Steven W. Graves *[a]

Acoustophoresis is a powerful technique for manipulating micro- and nanoparticles in microfluidic systems, but efficient particle capture remains limited by the size-dependent nature of the primary acoustic radiation force. This limitation has motivated the use of secondary acoustic forces to capture particles to wire meshes or larger suspended seed particles; however, these approaches are constrained by fluidic drag and limited control over particle residence time in acoustic fields. Here, we present an acoustofluidic capture strategy that combines primary and secondary acoustic radiation forces with laminar flow effects near surfaces to enable efficient microparticle trapping. Our device consists of a cylindrical microcapillary containing an axially aligned stainless-steel through-wire and an externally mounted piezoelectric transducer that generates an acoustic pressure node during flow. Microparticles are driven toward the wire by primary acoustic forces, where secondary acoustic interactions and reduced near-wall flow velocity promote stable capture. Devices with no wire, a centered through-wire, and an offset through-wire were evaluated to assess the role of wire placement within the acoustic field. Precise axial alignment of the wire with the pressure node yields optimal trapping, demonstrating a 3.6-fold increase in downstream particle concentration after cessation of the acoustic field, with overall capture efficiencies of 52–91%. This work establishes a design paradigm based on precise placement of microstructures within acoustic pressure fields to maximize particle trapping and capture in laminar flow systems.

Received 16th January 2026,
Accepted 2nd May 2026

DOI: 10.1039/d6lc00047a

rsc.li/loc

Introduction

Global plastic production has exceeded 8300 million metric tons since the 1950s, with more than 400 million tons produced annually and an estimated 60–80% ultimately discarded into landfills or the environment, including up to 4 million tons entering the oceans each year.[1–3] Over time, these materials degrade into micro- and nanoplastics (MNPs) that are now detected throughout the human body, including in blood, arteries, kidneys, placenta, and even the brain.[4–12] Although the full health implications remain under investigation, recent evidence links elevated microplastic accumulation to inflammation, metabolic disruption, neurotoxicity, and reproductive dysfunction, as well as correlations with neurodegenerative diseases such as dementia.[6,13,14] Beyond MNPs, biological nanoparticles such as exosomes and extracellular vesicles—naturally occurring particles of similar size to nanoplastics—play essential roles in intercellular communication and disease progression. The ability to efficiently isolate and analyze these biological particles from complex fluids is increasingly critical for advancing medical diagnostics and understanding disease mechanisms.[15] The overlap in physical properties and handling challenges between synthetic and biological nanoparticles underscores a shared need for improved, scalable separation technologies capable of precisely controlling nano- to micron-scale particles in flowing liquids.

Currently, techniques such as ultrafiltration, nanofiltration, and ultracentrifugation are commonly employed for the purification of MNPs from water.[16,17] While these approaches effectively remove particulates, each presents significant limitations. Filtration-based methods require high pressure differentials to drive flow through membranes, are prone to fouling, and rely on consumable filters that require frequent replacement.[17–19] Ultracentrifugation, though precise, is costly, energy-intensive, and limited to batch processing, making it unsuitable for large-scale or continuous applications.[20] Despite the widespread use of these methods in water treatment and industrial purification, residual particles are still detected in drinking water and commercial beverages.[21,22] Similarly, biological nanoparticles such as

[a] Department of Chemical and Biological Engineering, The University of New Mexico, Albuquerque, New Mexico 87131, USA. E-mail: graves@unm.edu
[b] Department of Pharmaceutical Sciences, College of Pharmacy, University of New Mexico Health Sciences, Albuquerque, NM, USA
[c] Department of Chemistry, New Mexico Institute of Mining and Technology, Socorro, NM 87801, USA
† Co-corresponding author.

exosomes and extracellular vesicles pose comparable isolation challenges, as existing ultracentrifugation and filtration-based techniques are laborious, low-throughput, and often yield impure fractions. The growing diagnostic and therapeutic importance of extracellular vesicles underscores the critical need for new, scalable isolation technologies that enable efficient, label-free isolation of nano- to micron-scale particles from complex liquid media.

Acoustophoretic separation has long been explored as a method for the removal of particles from fluids.[23,24] Acoustophoresis works by the application of an acoustic wave *via* mechanical vibration to a fluid under laminar flow conditions and allows for continuous flow and high separation efficiencies. Based on fundamental acoustic theory, particles subjected to an acoustic field in a fluid experience both a primary and secondary acoustic radiation force. The dependence of the primary and secondary forces on experimental parameters can be qualitatively understood by considering a 1D model.

The 1D equation for the primary acoustic radiation force is as follows,

$$F_P = -\left(\frac{\pi {p_0}^2 V_p \beta_f}{2\lambda}\right) \times \Phi(\beta, \rho) \times \sin(2kx) \quad (1)$$

$$\Phi(\beta, \rho) = \frac{5\rho_p - 2\rho_f}{2\rho_p + \rho_f} - \frac{\beta_p}{\beta_f} \quad (2)$$

where p_0 is the acoustic pressure amplitude, V_p is the volume of the particle, β_f is the compressibility of the fluid, λ is the wavelength, Φ is the acoustic contrast factor, k is the wavenumber, and x is the distance from the pressure node.[24] The primary acoustic radiation force is a time-averaged force largely driven by the size of the particle, the pressure amplitude, and the acoustic contrast of the particle to the surrounding media. The sign of the acoustic contrast factor (eqn (2)) dictates whether particles will move to the pressure node (positive) or the pressure anti-node (negative), where ρ_p is the density of the particle, ρ_f is the density of the carrier fluid, and β_p is the compressibility of the particle. In a capillary system, and in most real-world systems, the full three-dimensional formulation of the acoustic radiation force is more complex, but maintains the same qualitative behavior.[25] For the work presented here, the qualitative behavior is of most concern and as such we using the simpler 1D model to provide the framework for discussion of acoustic forces.

The secondary acoustic force is caused by the scattering of sound waves from particles and surfaces within the acoustic field, and either leads to attraction or repulsion of particles as a function of their interparticle distances and position within the acoustic field. The equation for the secondary acoustic radiation force is as follows,

$$F_S(x) = 4\pi a^6 \left[\frac{\left(\rho_p - \rho_f\right)^2 (3\cos^2\theta - 1)}{6\rho_f d^4} v^2(x) - \frac{\omega^2 \rho_f \left(\beta_p - \beta_f\right)^2}{9d^2} p^2(x)\right] \quad (3)$$

where a is the radius of the particle, d is the distance between the center of particles, ω is the applied resonant frequency, and θ is the angle between the center line of the particles and the direction of the propagating acoustic wave.[24] An attractive interparticle force is represented by a negative sign, while a repulsive interparticle force is represented by a positive sign. The first term on the right-hand side of the equation, dependent on the velocity amplitude of the particles ($v^2(x)$), is repulsive when particles are lined up in the direction of wave propagation (θ = 0°) and attractive when particles are aligned perpendicular to wave propagation (θ = 90°). Additionally, the velocity dependent term is at a maximum at the pressure nodes, and a minimum at the pressure anti-nodes. The second term on the right-hand side of the equation is dependent on the applied pressure amplitude ($p^2(x)$) experienced by the particles and is independent of particle orientation. The pressure amplitude term of the equation is always attractive while it diminishes in magnitude as it approaches the pressure node (minimum pressure).

Previous work has demonstrated the successful use of secondary acoustic forces to capture particles up to 1000 times smaller than the mesh size, and as a method to capture nanoparticles, exosomes, extracellular vesicles, and bacteria to micron-sized seed particles made of silica and polystyrene.[26–34] Although these approaches using secondary acoustic forces to entrap particles achieved separation of microparticles and nanoparticles from solution, they are generally limited by hydrodynamic drag, inability to precisely place structures for optimized particle capture, and inevitable saturation of particles to structures which minimizes overall throughput.

Inspired by earlier efforts in the field of acoustophoresis[25,35] we explore the use of both primary and secondary acoustic forces in a cylindrical microcapillary system for enhanced trapping and enrichment of MNPs. However, the work herein is fundamentally different than previous acoustophoretic studies, as we strategically position a high-gauge stainless-steel wire (50 μm diameter) parallel to the flow direction and centered on the axis of the microcapillary, placing the wire in the center of the predicted pressure node. We hypothesize that when the stainless-steel wire is positioned along the axial center of the microcapillary, suspended particles will be driven toward the acoustic pressure node through primary acoustic forces and will subsequently adhere to the wire surface through secondary acoustic forces (Fig. 1). Furthermore, the laminar flow profile produces relatively low axial velocities near the center of the capillary and in the immediate vicinity of the wire surface. Since convective transport scales with the local fluid velocity, particles in these regions experience weaker downstream transport. As a result, particles transported toward the wire have longer residence times near the trapping region, which promotes particle accumulation along the wire surface.

To test our hypothesis, we designed acoustofluidic devices using a cylindrical microcapillary with i) no through-wire

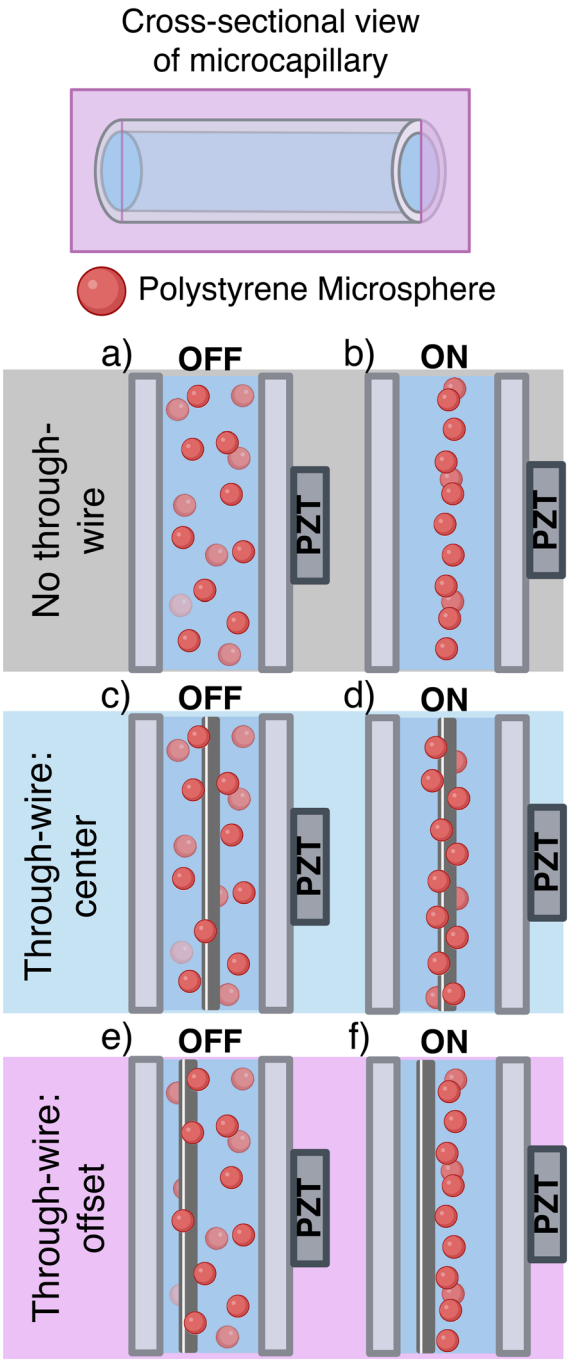

Fig. 1 Cartoon schematic of hypothesized acoustic focusing. A device without a through wire (a and b) exhibits particle focusing at the predicted pressure node. A device with an axially centered through wire (c and d) causes particle focusing at the pressure node and particles to become trapped at the wire surface. A device with an offset wire (e and f) will create particle focusing at the pressure node, undisturbed by the off-center positioning of the wire.

(Fig. 1a and b), ii) a centered through-wire (Fig. 1c and d), and iii) an offset through-wire (Fig. 1e and f), to evaluate acoustic focusing and trapping efficiency. We demonstrate *via* simulations and experimentally that microstructure placement within two-dimensional acoustic standing waves influences microparticle trapping efficacy. Moreover, the fixed nature of the axial wire prevents hydrodynamic drag on the trapping object from being a limiting factor in system performance. This work lays the foundation for designing acoustofluidic devices with optimally placed micron-sized wires for the improved enrichment and entrapment of microparticles. This work further suggests that the placement of fixed microstructures in standing acoustic waves may be an improved approach for the enrichment of nano and microparticles of many varieties, including biological particles.

Materials and methods

Acoustofluidic device construction

Two types of acoustofluidic devices were constructed using borosilicate glass capillaries: (i) devices without a through-wire and (ii) devices incorporating a through-wire. A picture of the acoustofluidic setup including all appropriate components and connections, along with the custom microfluidic device holder, is shown in Fig. 2a. For devices without a through-wire, a lead zirconate titanate (PZT) ceramic discs (20 mm × 2.7–3 mm, STEMiNC, Davenport, USA) was attached to a borosilicate glass microcapillary (1.12 mm ID, 2 mm OD, 1B200-4, World Precision Instruments, Sarasota, FL) *via* super glue (Professional Liquid, Loctite, Westlake, OH) and allowed to cure for 24 hours. SILASTIC™ tubing (0.76 mm ID, 1.65 mm OD, The Dow Chemical Company, Midland, MI) was attached to the branched opening of a microfluidic T-junction (PEEK Low Pressure Tee Assembly, 1/16″, 0.020 thru hole, P-712, IDEX, Oak Harbor, WA) to serve as the inlet and outlet of the device, and the layout of the inlet and outlet are mirrored versions of each other. Flat bottom plugs (Plug PFA, ¼-28, flat bottom, P-316, IDEX) were attached to one end of the main pipeline of the T-junction, and stainless-steel tubing (0.04″ ID, 1/16″ OD, 5 cm length, IDEX) was attached to the other end. The borosilicate glass microcapillary with the PZT was then attached to the stainless-steel tubing of both the inlet and outlet *via* silicone tubing. The SILASTIC™ tubing from the outlet T-junction was attached to a female Luer lock (Female LuerTight™ fitting system, 1/16″ OD, P-835, IDEX).

Acoustofluidic devices with a through-wire were constructed similarly, but with a modification to the end plugs of the T-junction. Custom made plugs (¼-28) were 3D printed with a through-hole approximately 350 μm in diameter. A small piece of rubber was super-glued to the end of the custom plug that would be inserted into the main pipeline of the T-junction. A 30-gauge needle was then inserted in the through hole of the custom plug and ultimately through the glued piece of rubber. A stainless-steel wire (44 AWG, 316L, 0.002″, Remington Industries, Johnsburg, IL) was carefully threaded through the 30-gauge needle until the wire was completely through the modified plug. At this point, the stainless-steel wire (diameter = 50 μm) was gently pulled through the modified

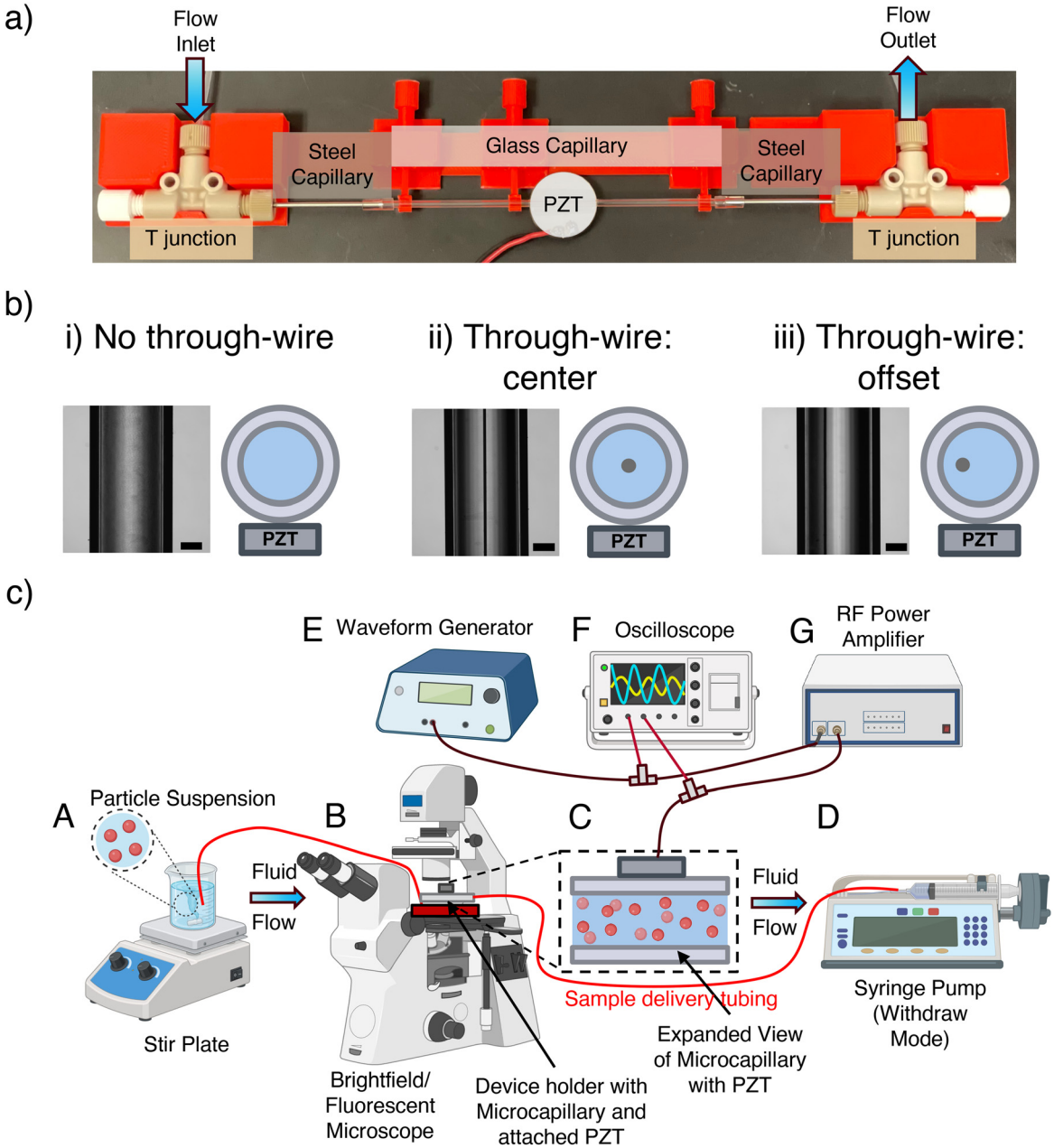

Fig. 2 a) Image of the microfluidic device mounted in the device holder. b) Cartoon representation and brightfield images of all three devices in cross-sectional view. c) Process flow of the acoustofluidic set-up. Fluid flow is represented by blue arrows, which is the direction of flow through the sample tubing (red line), while electrical connections are shown by black wires. PS microspheres were mixed in a conical tube with a stir bar (A) and flowed upstream through the microcapillary device placed sitting on an epi-fluorescent microscope (B). An expanded view of the capillary is shown (C). Fluid flow was driven using a syringe pump set to 'withdraw' mode (D). The acoustic focusing field was applied in the glass microcapillary *via* the PZT, operated by a radio frequency power amplifier (G), and the frequency driven by a waveform generator (E). The waveform generator and radio frequency power amplifier were connected *via* an oscilloscope (F).

plug and threaded through the inlet T-junction, steel tubing, glass microcapillary, steel tubing, outlet T-junction, and finally another modified plug on the outlet T-junction. The stainless-steel wire was positioned along the axial centerline of the capillary and maintained under tension to ensure stable alignment during operation. The wire was tensioned using two 20 g masses attached to its ends, producing an estimated axial tension of approximately 0.39 N (F = mg). Under these conditions the wire remained straight within the capillary during acoustic excitation, with an estimated fundamental resonance frequency of approximately 800 Hz.[36] As the resonance frequency of the taut wire is roughly three orders of magnitude lower than the ultrasonic excitation frequency used in this work (~800 kHz), the wire behaves as a rigid inclusion relative to the acoustic wavelength.

Microfluidic device holder

For all devices tested, a custom designed and 3D printed microfluidic holder was constructed to properly hold each device. Inserts were designed to hold both the inlet and outlet T-junctions, as well as ensure that these T-junctions remained in-line with each other *via* a dove tail sliding rail. Sliding tube holders were also designed to be placed along the railing system, and support the glass capillary at various points across its length. Additionally, inspired by the design of a micrometer, these tube holders also served as aligners of the glass microcapillary to assist in either placing the stainless-steel through-wire in the center or off-center for the appropriate experiments. All configurations of this experimental design are shown in Fig. 2b, demonstrating a microcapillary with i) no through-wire, ii) a centered through-wire, and iii) an offset through-wire.

Acoustic focusing in microcapillary devices

A process flow diagram of the experimental setup is shown in Fig. 2c. Devices were rinsed with 20% Contrad 70 (Decon Labs, King of Prussia, PA) prior to testing to mitigate non-specific adherence of microparticles to the device. All experiments were conducted using high intensity fluorescent Nile red polystyrene (PS) microspheres at ~150 000 particles per mL (10.0–14. 0 μm, FH-10056-2, Spherotech, Lake Forest, IL). PS microspheres were mixed in a conical tube with a stir bar (A) and flowed downstream through the microcapillary device (C) sitting on a Nikon Eclipse Ti-U microscope (B) (Nikon, Melville, NY). Experiments were performed at a flow rate of 200 μL min^{-1} using a 10 mL syringe (Air-Tite, Virginia Beach, VA) and syringe pump (fusion 200× high-precision syringe pump, Chemyx, Stafford, TX) set to 'withdraw' mode (D). For the operating flow rate of 200 μL min^{-1} in a capillary with an inner diameter of 1.12 mm, the average fluid velocity is approximately 3.4×10^{-3} m s^{-1}, corresponding to a Reynolds number of Re ≈ 3.8 (using water properties ρ = 1000 kg m^{-3} and $\mu = 1.0 \times 10^{-3}$ Pa s), confirming that the flow remains well within the laminar regime for all wire configurations investigated. The acoustic focusing field was applied perpendicular to the flow in the glass microcapillary *via* the PZT, operated by a radio frequency power amplifier (G) (model 320L, E&I, Rochester, NY), and the frequency driven by a waveform generator (E) (33220A, Agilent, Santa Clara, CA) set to 50 mV. The waveform generator and radio frequency power amplifier were connected *via* an oscilloscope (F) (DS1102E, RIGOL, Portland, OR) to determine the peak-to-peak applied voltage (V_{pp}). For all experiments, V_{pp} applied was between 52.4–53.2 V.

Video acquisition and imaging

Videos were acquired for the device without a through-wire, with an axially centered through-wire, and an off-center wire with an ORCA®-Flash 4.0 CMOS camera (Hamamatsu, Bridgewater, NJ) mounted to a Nikon Eclipse Ti-U microscope (Nikon, Melville, NY) using a 4X objective. For epi-fluorescent videos, PS particles were excited with a 10 W green LED flashlight (UltraFire, Amazon) mounted to the collimating adapter on the microscope, and ultimately using a filter cube set with a 545/30 band-pass filter for excitation. Brightfield videos were captured with an exposure time of 10 ms. Both fluorescent and brightfield videos were captured using HCImage software (Hamamatsu, Sewickley, PA) with a time scan set to capture an image every 500 ms for 20 seconds, including an image at t = 0 seconds. For all devices, videos were acquired with the PZT off, PZT on, and immediately after the PZT was turned off.

COMSOL Multiphysics modeling

All COMSOL Multiphysics models were performed in version 6.3 and 6.4. The study physics used (as described below) were the eigenfrequency study and the laminar flow study (stationary). The model geometry was constructed within COMSOL to dimensions matching the experimental systems. Materials properties were taken from literature references and manufacturer specifications and are given in Table 1.[37–42] The 2D models were created using standard COMSOL CAD tools and the geometries for each model are shown in Fig. S2. The 3D models were created using simple cylinders to represent sound-hard boundaries and sound-soft boundaries for the pressure acoustics eigenfrequency study and no slip walls, as well as the inlets and outlets for the laminar flow studies (Fig. S1). All models were meshed using a physics-controlled mesh based on the physics used in the COMSOL study. For the 2D pressure acoustics eigenfrequency study extremely fine element sizes were used in the mesh (Fig. S2). For the 3D models, the mesh element size was fine for the eigenfrequency study and finer for the laminar flow study (Fig. S1). For all eigenfrequency studies, the temperature was modeled at 20 °C. For the laminar flow studies, the inlet flow was set to a fully developed volumetric flow rate of 200 μl min^{-1}.

Table 1 Material properties used for COMSOL Multiphysics 2D and 3D models

Material	Speed of sound (m s^{-1})	Density (kg m^{-3})
PZT	5500	7800
Superglue[a]	3250	1060
Glass[b]	5500	2300
Stainless steel	5800	7930
Water	1485[c]	998[c]

[a] These values are expected to vary slightly brand to brand based on specific polymer makeup. Commercial superglue is commonly a combination of poly(methyl cyanoacrylate) (PMCA) or poly(ethyl cyanoacrylate). [b] These values were calculated from the manufacturer provided values for the density and Young's modulus of Kimble N51A glass, which is the glass that our capillaries are constructed from. [c] These values are taken from the COMSOL Material Library for the simulation. The specific values shown in the table are for fresh water at 1 atm and at 21 °C. The values for temperature are calculated as in (4) and density as in (5). The actual simulation uses values as calculated in COMSOL, which are expected to be nearly identical.

Video analysis

Gaussian fit for focusing width. To determine the focusing width across the devices, a Gaussian curve was fit to the intensity profile of particles flowing through the microcapillary for all devices where the PZT was either off or on. Videos were acquired using a 500 ms exposure time for a total of 20 seconds. MATLAB (Mathworks®, Natick, MA) was used to upload a multiple-page tif file consisting of a series of 16-bit images. A composite image based on the average projection of each image was created and a predetermined region of interest (ROI) of 500 pixels thick centered on the image was used for the analysis. Within the ROI, the intensity of each column of pixels was averaged to minimize the noise across all the images, creating an averaged single intensity value for each column, and ultimately an averaged intensity plot for the composite image (Fig. 6a and b). From the averaged intensity plot, the data was baseline corrected and binned every 10 μm across the *x*-axis to further minimize noise. A series of Gaussian curves were fit to the intensity profile, with a minimum of one Gaussian curve for each profile dependent on the distribution of particles. Some data sets with multiple peaks were fit to more than one Gaussian curve, which were summed together to achieve a combined profile. The final composite Gaussian curves were normalized to the maximum intensity value to allow direct comparisons of all experiments. For each set of experiments, the microcapillary was not in the exact same position within the camera field of view. To account for any misalignment across experiments, Gaussian curves where the PZT was off were corrected along the *x*-axis by setting the maximum peak intensity value to an *x*-position of zero. For Gaussian curves where the PZT was turned on, the positioning was corrected in the following ways. The Gaussian curve for the device without a through-wire was set to an *x*-position of zero where the peak intensity was at a maximum. For the device with the axially centered through-wire, the Gaussian curve was set to an *x*-position of zero between the two intensity maxima, as these peaks represented the edges of the through-wire. Finally, the Gaussian curve of the device with the offset wire was set to an *x*-position of zero where the intensity of the focused particles was at a maximum.

Calculating the sum of the raw pixel intensity after immediately turning the PZT off. The sum of the pixel intensity within a ROI was used to evaluate the effects of acoustic focusing and acoustic trapping immediately after the PZT was turned off. For these experiments, the PZT was on for a duration of 15 seconds, 30 seconds, 1 minute, or 2 minutes, to evaluate the temporal effects of particle trapping with all three devices (n = 3 per device). The PZT was only run for a few minutes at a time continuously, and shut off between subsequent experimental runs to avoid overheating the system. Epi-fluorescent videos were acquired at 490 ms exposure time for 24 seconds immediately after the PZT was turned off. MATLAB was used to upload a multiple-page tif (mptif) file consisting of a series of 16-bit images. An ROI was chosen to encapsulate the entirety of the inner portion of the microcapillary. For each image in the mptif file, the sum of the raw pixel intensities within the ROI was calculated. The area under the curve of the sum of the raw pixel intensity graphs was calculated for all devices and experimental conditions to correlate to particle concentration.

Results

The foundation of this work is based on the use of cylindrical microcapillaries to create resonant structures that have an acoustic pressure node at the axial center of flow.[35,43,44] Once excited by the PZT, acoustic energy propagates along the fluid-filled capillary and can establish standing-wave pressure fields that extend beyond the immediate footprint of the transducer, allowing particle focusing to occur over a larger length of the axial region of the channel, as previously observed in capillary-based acoustic focusing systems.[25] It is expected at larger distances from the transducer the focusing is weaker and less understood, due to radial propagation of acoustic waves from the edge of transducer. Acoustic flow cytometry utilizes the same technique by using the primary acoustic force to drive particles to a central node where they are further analyzed optically. Here we use the same basic structure (Fig. 1a and b) but have additionally placed a wire in the predicted axial central acoustic pressure node (Fig. 1c and d). In this position, we hypothesized that the primary force would still drive the particles to the center, and that the secondary acoustic force would trap microparticles to a methodically placed micron-sized wire (Fig. 1d). Although these principles of a 2D acoustic standing wave in a cylindrical microcapillary are well characterized, the effect of placing a wire in the axial center of the pressure node was unknown. We hypothesized that in the absence of an acoustic standing wave, all devices (without the wire, with an axially centered wire, and with an offset wire) would exhibit an unfocused spread of microparticles throughout the microcapillary (Fig. 1a, c and e). In the presence of an acoustic wave at an optimum drive frequency without a through-wire, we expected microparticles to acoustically focus at the central node, as is the basis for numerous acoustic flow cytometry devices (Fig. 1b). With a centered through-wire and an optimum drive frequency, we hypothesized microparticles would be driven to the pressure node based on the primary acoustic force, and adsorb to the wire *via* the secondary acoustic force, which would be further assisted by the near zero flow velocity next to a no slip wall due to the wire presence (Fig. 1d). We further hypothesized that with an offset wire in the microcapillary system and an optimum drive frequency, the system would focus particles at the central node similar to the device without the through-wire, as the thin wire (50 μm diameter) would have a minimal impact on acoustic focusing (Fig. 1f).

COMSOL Multiphysics was used to create models of dimensionally accurate flow and pressure profiles using corresponding material properties and experimental

conditions. To evaluate the effects of both the presence and positioning of a through-wire within a borosilicate microcapillary device, 2-dimensional and 3-dimensional flow profiles were simulated using COMSOL and demonstrated unique differences for microfluidic devices without and with the wire (Fig. 3). The simulation of the microfluidic device without the through-wire predicted maximum flow at the center of the microcapillary, with a minimum flow at the tube walls due to no-slip boundary conditions (Fig. 3a, d and g). The microfluidic device with the axially centered stainless-steel through-wire predicted two regions of minimum flow located at the tube wall and the outer edge of the stainless-steel through-wire, while the flow maximum is predicted to be between these

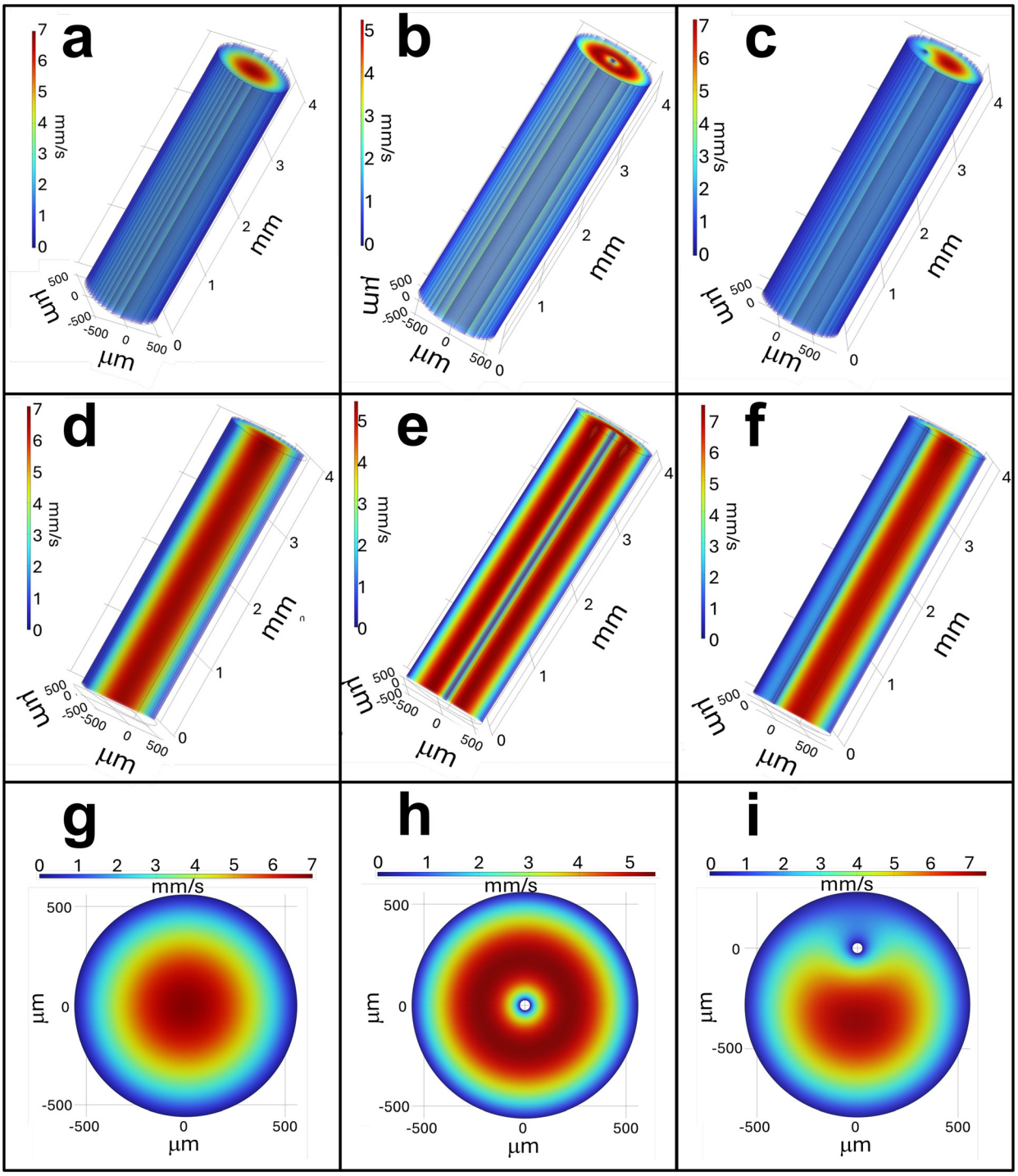

Fig. 3 A 3-dimensional (a–f) and 2-dimensional (g–i) COMSOL modeling of predicted flow profiles without a through wire (a, d and g), with a through-wire at the axial center (b, e and h), and with a through-wire off-centered (c, f and i).

two regions (Fig. 3b, e and h). The microfluidic device with the offset wire predicted a flow profile similar to the device without a through-wire, but with an expansion on one side of the microcapillary of the minimum flow profile due to the proximity of the through-wire to the tube wall (Fig. 3c, f and i). Notably, the maximum predicted fluid velocity achieved for each respective device is lowest with the centered through-wire (~5.5 mm s^{-1}), followed by no through-wire (~7 mm s^{-1}) and the offset wire (~7.5 mm s^{-1}). From the 2-dimensional COMSOL models predicting the acoustic focusing pressure node formation, all devices maintain nearly identical pressure profiles with minimal differences in predicted resonant frequencies (Fig. 4). These simulations show that in all three experimental conditions, a central pressure node is predicted to form at frequencies similar to those used in the experimental work. Although the capillary system with the attached PZT is asymmetric, the simulation predicts two orthogonal pressure profiles with respect to the capillary both horizontally and vertically. Though the two pressure modes occur at slightly different frequencies (<Δ2 kHz), this suggests that a pressure minimum would form at the axial center of the capillary, which is consistent with modeling of similar systems.[25,45]

To evaluate our acoustic focusing and flow models, we constructed a microcapillary devices without a wire, with a centered wire, and with an offset wire. We used these to capture videos of microparticle flow with and without a resonant acoustic standing wave. Fig. 5 shows representative images of fluorescent and brightfield videos with the three experimental conditions: no through-wire, centered through-wire, and an offset through-wire. For all experimental conditions, microparticle flow in the absence of acoustic waves demonstrated a similar non-specific, unfocused flow pattern (Fig. 5a, c and e). As expected, in the absence of a through-wire, microparticles were successfully driven to the center of the microcapillary with an optimum drive frequency by the PZT (Fig. 5b). Notably, in the presence of a centered through-wire and an optimum drive frequency, microparticles successfully collapse to the through-wire and experience acoustic trapping (Fig. 5d). Specifically for the fluorescent image with the through-wire, the wire is visibly illuminated with microparticles with little to no particle presence in the bulk media. Interestingly for the device with

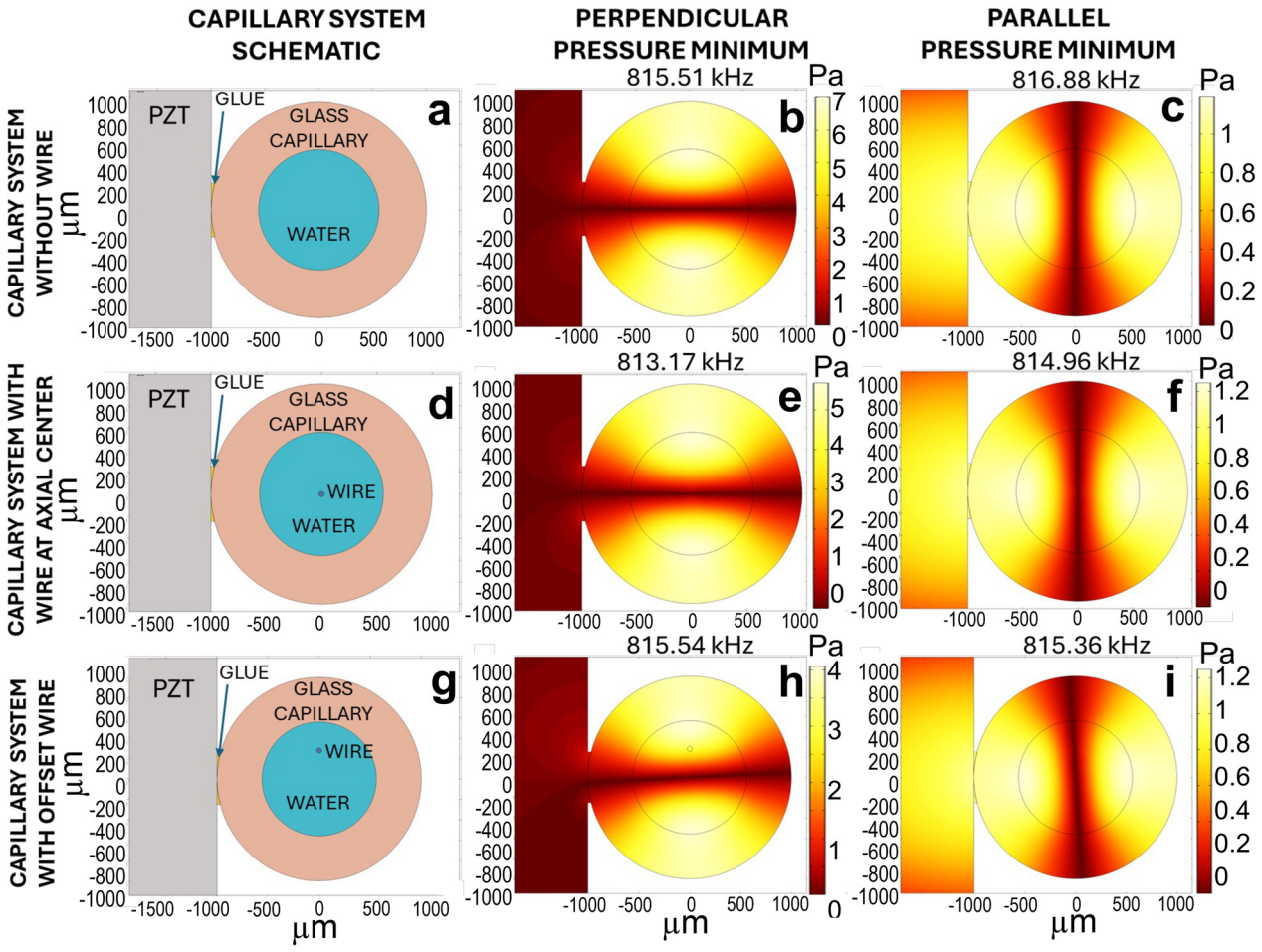

Fig. 4 A 2-dimensional COMSOL modeling of predicted acoustic pressure profiles without a through-wire (a–c), with a through-wire at the axial center (d–f), and with a through-wire off-centered (g–i).

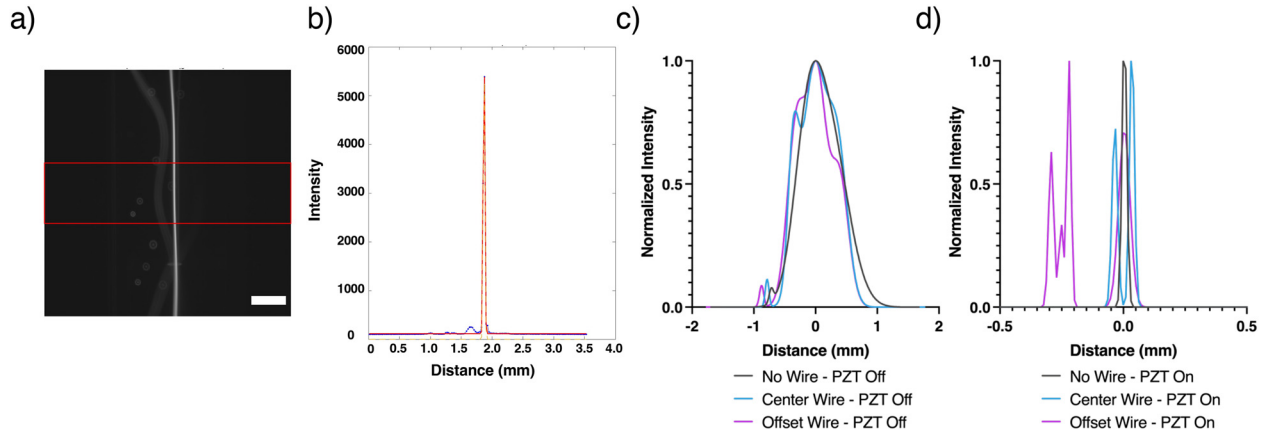

Fig. 5 Generation of fluorescence intensity profiles of particle distributions across three device configurations, derived from captured video recordings. (a) Definition of the region of interest (ROI) shown by the solid red lines (scale bar = 500 μm) and b) the corresponding Gaussian fit for the intensity profile from the composite image. c) Particle distributions for the three device configurations under acoustic-off conditions. d) Corresponding particle distributions under acoustic-on conditions.

the offset through-wire and an applied drive frequency, microparticles are both trapped to the through-wire and achieve a streamlined acoustic focusing at the center of the microcapillary (Fig. 5f).

To better quantify the differences in acoustic focusing behavior for all devices, Gaussian curves were fit to the intensity profiles for fluorescent videos with the PZT off or on (Fig. 6). A composite image of all frames from the video was created and the ROI was drawn in a solid red line for a qualitative understanding of the image quantification (Fig. 6a). The averaged intensity profile, represented by the blue markers, was then fit to a Gaussian curve, shown as the solid red line, across the entire composite image (Fig. 6b). The presence and position of the through-wire, in the absence of an acoustic drive frequency, does not significantly impact microparticle positioning (Fig. 6c). Specifically, all three devices demonstrate similar widths across their respective Gaussian profiles, suggesting that the presence of the wire does not innately alter microparticle positioning. The drive frequencies of all three devices could be manually tuned to use acoustic standing waves that focused particles to the axial center of the capillary (Fig. 6d). In the device without the through-wire, there is one visible peak due to particles focusing at the pressure nodal plane of the microcapillary as expected. For the device with the centered through-wire, two intensity peaks are present that represent the edges of the stainless-steel wire. However, both peaks are centered around the location of the centered through-wire. Notably for the device with the offset through-wire, two distinct clusters of peaks appeared. The first peak centered at the middle of the microcapillary (distance = 0.0 mm) is due to the acoustic focusing of particles to the pressure nodal plane from the drive frequency. The second cluster of peaks is centered around the offset through-wire (distance = −0.25 mm) and represents particles trapping to the wire in the presence of the acoustic field.

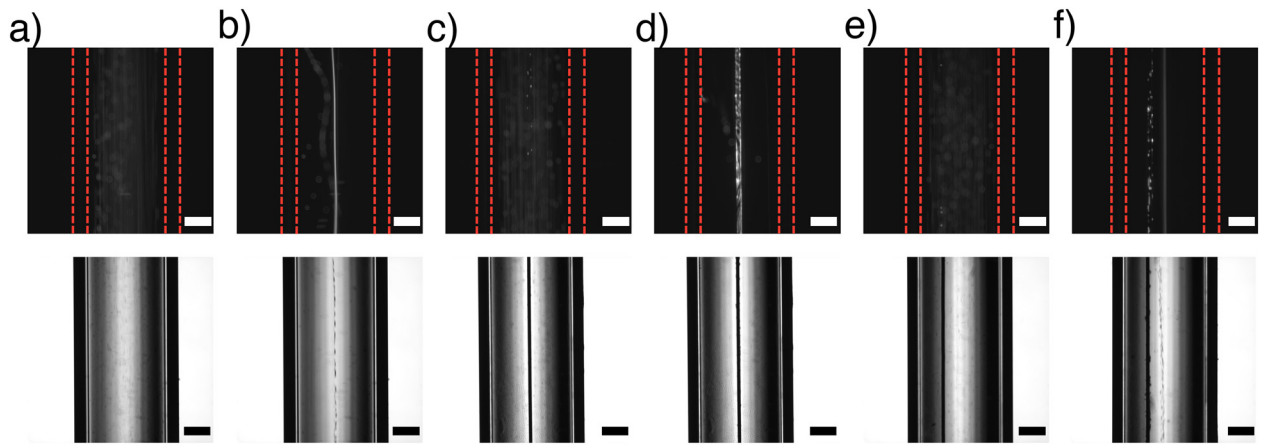

Fig. 6 Representative fluorescent and brightfield images of particle flow through the microcapillary with the PZT off and the PZT on with no wire (a and b), a centered through-wire (c and d), and an offset through-wire (e and f), respectively. Scale bars for both fluorescent images (white scale bars) and brightfield images (black scale bars) are shown at the bottom right of each image and represent 500 μm.

As the PZT was turned off, we observed a large flux of particles in the field of view for the device with the centered through-wire, while the device without the through-wire and the offset wire did not show noticeable differences in particle concentration (Fig. 7). More specifically, after the PZT was immediately turned off, a series of snapshots demonstrates that the device with a centered through-wire showed an increase in particle concentration as the acoustic force was no longer applied (Fig. 7a and S4). To quantify the differences in particle concentration, the sum of the pixel

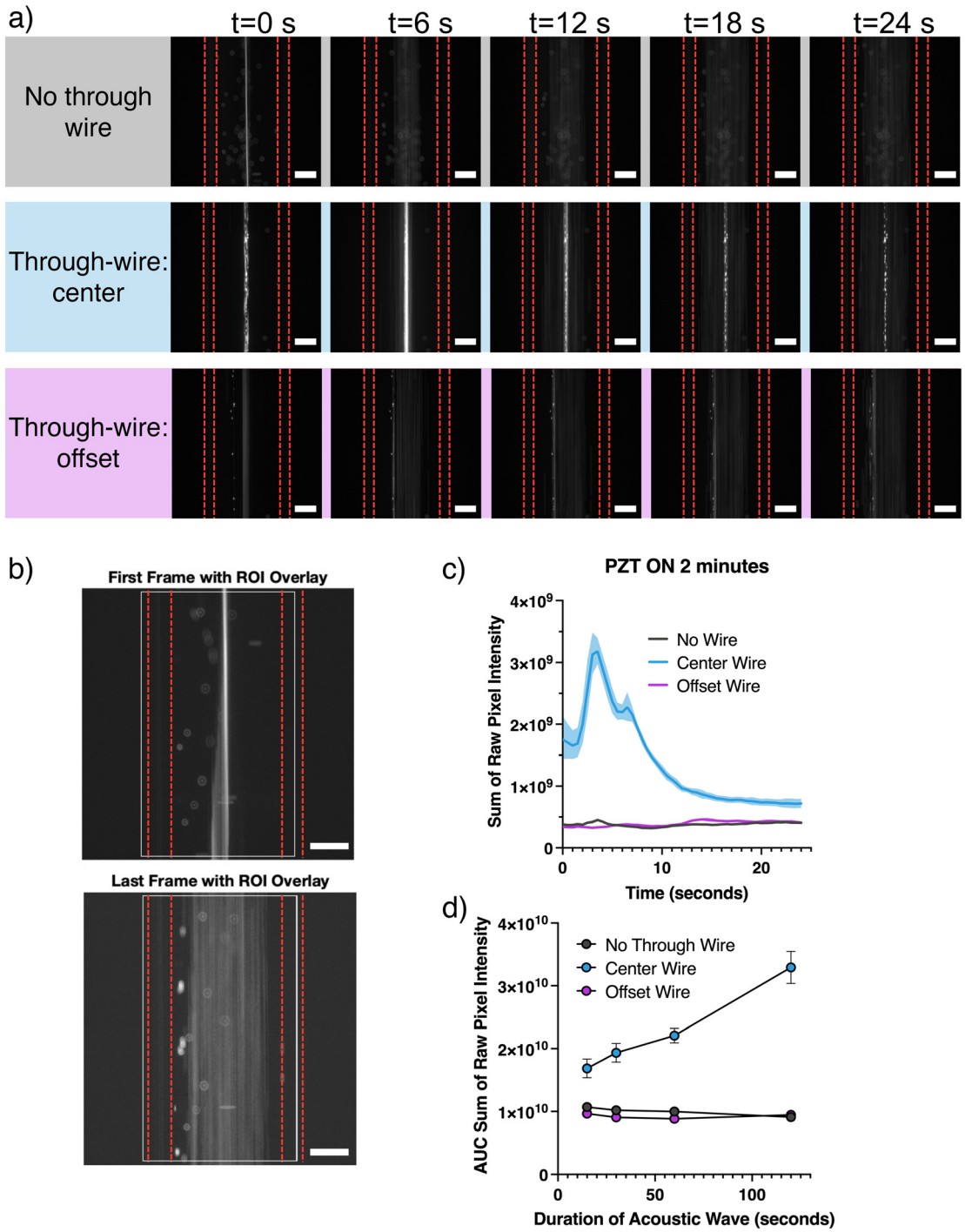

Fig. 7 a) Representative panel images over time immediately after the PZT is turned off without a through-wire, with the through-wire centered, and the through-wire offset. The PZT was on for a duration of 1 minute prior to turning off. The tube walls are represented by dashed red lines. b) Visualization of the ROI used to process the video frames immediately after the PZT was turned off shown with the solid white line. c) Sum of the raw pixel intensity of the video frames immediately after the PZT was turned off after the PZT was on for 2 minutes. d) Area under the curve (AUC) for the sum of the raw pixel intensities for all durations of the PZT being on. All graphs display the mean with standard deviation (n = 3). Scale bars = 500 μm.

intensity within a ROI was used for each frame across the time series and baseline corrected to observe the change in fluorescence intensity over time (Fig. 7b). Since the accumulation of particles on the devices with the through-wire was expected to vary as a function of time, we examined the temporal effects by turning the PZT on for 15 seconds, 30 seconds, 1 minute, and 2 minutes, prior to analyzing the particles after immediately turning the PZT off. As the experiments were conducted with the same particle concentration and volumetric flow rates, the sum of raw pixel intensity was directly correlated to the relative concentration of particles flowing through the microcapillary. As such, increases in raw pixel intensity within the ROI over time directly reflect increases in particle concentration, suggesting particle trapping occurred upstream as videos are taken immediately after the acoustic force is removed. Plotting the sum of the raw pixel intensity values for each microfluidic device across the time series shows that the devices without the through-wire and the offset wire maintain a relatively consistent concentration of particles, while the devices with the centered through-wire observes an increase in particle concentration over time (Fig. 7c and S5). As the application time of the acoustic wave was increased from 15 seconds to 2 minutes, the device with the centered through-wire experienced a drastic increase in the sum of raw pixel intensity, highlighting effective trapping of particles to the wire (Fig. 7c and S5). Specifically for the case where the acoustic wave was present for 2 minutes prior to being turned off, the initial sum of the raw pixel intensity ($t = 0$) for the device with the centered through-wire was 4.6 times greater than the device without the through-wire, demonstrating acoustic trapping of particles to the through-wire within the ROI during this time period (Fig. 7c). When calculating the area under the curve for all durations of the PZT turned on (15 seconds, 30 seconds, 1 minute, and 2 minutes), the device with the through-wire shows a distinct increase in particle concentration (in the frames collected after the wave was turned off) as a function of time, achieving 3.6 times greater concentration of particles (Fig. 7d). These results further support our hypothesis that efficient acoustic trapping occurs on the centered through-wire. The observed increase in particle concentration after the PZT is turned off arises from particles upstream that are no longer retained once the acoustic forces are removed.

Discussion

The objective of this study was to investigate the acoustic trapping of microparticles by strategically positioning a micron-sized wire within a microfluidic channel and applying acoustic standing waves to achieve effective microparticle trapping under laminar flow conditions. First, we successfully designed and constructed a novel microfluidic device that allows for the accurate positioning of a 50 μm diameter stainless-steel through-wire within a cylindrical microcapillary (Fig. 2a). Specifically, the microfluidic device holder allows the wire to be placed in the desired location within the microcapillary to investigate particle focusing (Fig. 2b). Previously designed devices for investigating the separation of particles *via* secondary acoustic forces consisted of flow chambers with aluminum mesh, polymer mesh, millimeter-scale glass beads, stainless-steel wires perpendicular to flow, and PS seed particles.[26,28,29,46,47] Most of these systems consist of highly unorganized structures and random packing within the flow device, potentially affecting their maximum trapping efficacy. Next, we demonstrated that precise axial placement of a stainless-steel through-wire within a microcapillary enhances particle enrichment through both primary and secondary acoustic forces, while also promoting particle trapping by taking advantage of reduced flow velocities near no-slip boundaries under laminar flow. The efficiency of particle trapping was evaluated through a combination of experimental observations and COMSOL Multiphysics simulations.

COMSOL Multiphysics was used to model both flow profiles and pressure profiles of the microcapillary devices without and with the wire based on accurate physical and material properties (Fig. 3 and 4). Laminar flow profiles without a through-wire predicted maximum fluid velocity at the center of the microcapillary and minimum fluid velocity at the capillary wall due to no slip boundary conditions. As expected, both devices with the through-wire showed minimum velocity at the tube wall and the edge of the stainless-steel through-wire. Interestingly, the positioning of the predicted pressure nodes for all device configurations—whether or not a through-wire is present—are nearly identical, indicating that the wire has minimal influence on the acoustic focusing pattern. Early models of acoustic pressure nodes in cylindrical systems predicted the presence of multiple lobes around the center of the capillary cross-section, where positive-contrast particles were expected to focus.[25] A later acoustic pressure model predicted an asymmetrical acoustic pressure profile, with stronger pressure gradients on the same axis as the piezo transducer.[45] Interestingly, the eigenmode study of acoustic pressure nodes modeled in COMSOL for this study predicts two potential resonant standing wave structures that occur at very similar frequencies. One is perpendicular to the drive surface PZT and the other is parallel to that surface (Fig. 4). Since these predicted perpendicular and parallel pressure profiles exist at nearly identical frequencies, it is possible that they exist nearly simultaneously within the same system and alternate between both modes, leading to an enhanced focusing at the center of the capillary. As acoustic focusing depends on both the capillary dimensions and the temperature of the carrier fluid, it is possible for multiple acoustic modes to coexist. This may arise from slight variations in the capillary's inner diameter as well as temperature gradients within the fluid caused by heat transfer from the PZT.[48]

We initially hypothesized that acoustic focusing would occur in all three device configurations, as illustrated in

Fig. 1. Visualization of brightfield videos, along with quantitative analysis of fluorescence recordings under acoustic-off and acoustic-on conditions, generally confirmed this hypothesis (Fig. 5). As expected, acoustic focusing in the capillary device without a through-wire closely resembled the behavior previously reported for glass and steel cylindrical devices.[25,35] In contrast, in the device containing the centered through-wire, particles were trapped on the wire surface and moved downstream along the wire by the fluid flow. Due to the presence of the wire at the center of the acoustic pressure node, particles never truly reach the predicted pressure minimum and are offset by the radius of the wire. As such, the applied pressure amplitude term ($p^2(x)$) in the secondary acoustic radiation force equation does not completely diminish, although it achieves a minimum relative to other radial positions in the microcapillary. Under normal acoustic flow conditions in a cylindrical capillary, the particles would achieve a maximum velocity at the pressure node. However, the velocity amplitude of the particles ($v^2(x)$) at the pressure node in the presence of a centered through-wire approaches zero due to no slip boundary conditions along the wire (eqn (2)). In the presence of the centered through-wire and acoustic excitation, particles focused toward the wire, where some became acoustically trapped on the wire surface while others remained suspended and continued to flow along its length. In contrast, with the offset through-wire configuration, two behaviors are observed simultaneously: a fraction of particles is acoustically trapped at the wire surface, while the remainder are acoustically focused to the central pressure node and transported downstream along the nodal plane (Fig. 5f and 6d). When acoustic forces are applied, particles flowing through the microcapillary in the vicinity of the offset through-wire are first driven towards the pressure node *via* the primary acoustic force. As the distance between the microparticles and the offset through-wire decreases, the secondary acoustic force aids in particle trapping to the wire surface due to attractive secondary forces. While additional forces such as surface-to-surface attraction certainly also have an effect, the fact that removal of the acoustic standing wave results in large scale release of particles from the surface implies that the combination of acoustic forces and wire positioning are the primary driver of particle adherence to the wire surface.

Interestingly, the presence and positioning of the wire did not disrupt the standing acoustic wave formed, demonstrated both *in silico* and experimentally. When a solid layer is very thin compared with the wavelength of sound in the surrounding fluid, it does not behave as a medium through which sound propagates with appreciable phase accumulation. Instead, it behaves effectively as a small surface mass. In this long-wavelength limit, the acoustic field experiences negligible phase change across the layer and internal interference effects within the solid do not develop. Within this experimental setup, as the wire diameter is small relative to the acoustic wavelength, the structure cannot support significant spatial variations in acoustic phase and the standing-wave field within the cylinder remains essentially unchanged. As a result, transmission is high and perturbation of the incident wave is minimal.[36] However, the lack of acoustic wave perturbation in the system due to the wire presence does not exclude the wire from participating in the scattering of the incident acoustic waves. Both the microspheres and the wire participate in Rayleigh scattering, defined for objects whose diameters are much smaller than the wavelength of the incident sound ($d < \lambda/10$).[49] As such, the resulting scattered waves influence the secondary acoustic forces that lead to trapping of particles along the wire.

Similar acoustic trapping behavior was observed for mesh filtration systems when acoustic forces are applied to particles flowing through the system, as particles in proximity to the mesh structure adhere to the mesh even though they are up to 1000 times smaller than the mesh size.[28,29] Secondary acoustic forces have also been observed in systems with larger seed particles retained at the pressure nodal plane *via* high acoustic forces, where the suspended smaller particles experienced a diverted path towards the direction of the seed particles.[50,51] In a simplified singular wire system modeling a complex acoustic mesh, particles that were located near a pressure node experienced a diversion of their flow patterns towards the wire structure at close enough distances, demonstrating that secondary acoustic forces affected particle flow directions in proximity to wire surfaces.[46] Notably, this system used wires that were aligned perpendicular to the flow direction and parallel to the direction of the standing wave, which is opposite of the microcapillary system that we have created here. In our system, the wire is parallel to flow and its surface is perpendicular to the standing wave. Assuming that the surface of the wire can be approximated as the surface of a microparticle, this conceptually ensures that the secondary force is effectively always attractive to the wire as particles flow in parallel flow streams past it. Such a configuration is expected to be beneficial for particle enrichment and potential alignment processes useful for a variety of analyses techniques.

The expression used here for the secondary acoustic interaction force is derived for sphere–sphere interactions of the same size and material properties, and therefore does not explicitly account for the cylindrical geometry or material properties of the steel wire. Existing theoretical treatments of secondary acoustic radiation forces have primarily focused on interactions between spherical particles, and analytical descriptions of sphere–cylinder interactions at the microscale relevant to this system remain limited.[52,53] Recently, more in-depth mathematical expressions have been derived describing the secondary acoustic forces for particles of different sizes and material properties.[50,54,55] In the present work, we employ the sphere-sphere formulation as a first-order approximation to qualitatively describe the interaction between suspended particles and the nearby wire surface. The experimentally observed aggregation of particles to the

wire surface is therefore qualitatively consistent with secondary acoustic interactions of this type, although quantitative differences are expected due to the cylindrical boundary and the mechanical properties of the wire. A more rigorous theoretical treatment of sphere–cylinder secondary acoustic interactions represents an important direction for future work.

For the device with a centered through-wire, an increase in particle concentration and intensity was observed when the PZT was immediately turned off (Fig. 7). After quantifying the intensity as a function of time after turning the PZT off for all three devices, the device without the through-wire maintained a relatively constant intensity profile over time for all durations of the acoustic wave presence. This result confirms that there was not particle accumulation throughout the device as the acoustic signal was turned on, as the intensity remained relatively constant and therefore the concentration of particles remained constant as well. For the device with the offset wire, no change in intensity was observed over time for all PZT conditions, suggesting a little to no microparticles were entrapped while the PZT was on. Most notably, the device with the centered through-wire saw an increase in the AUC of the sum of the pixel intensity for all PZT on durations tested, highlighting particle trapping to the centered through-wire (Fig. 7d). Interestingly, the device with the centered through-wire experienced increasing initial intensity values as the duration of the acoustic wave presence increased. This increase in intensity as a function of the duration of the PZT being on, specifically for the PZT being on for 2 minutes, could be due to a partial saturation of particles adsorbing to the wire further upstream. As such, over the course of the 2 minutes, particles continue to adhere to the centered through-wire and result in a greater initial intensity value within the measured ROI for the frame just prior to the acoustic field being turned off. Using the intensity profiles shown in Fig. 7 and S5, we sought to further estimate the number of particles successfully trapped to the centered through-wire, as detailed in the SI. Briefly, the videos of the device without the through-wire were used to estimate the total number of particles represented by the AUC, using the volumetric flow rate and particle concentration. The number of particles relative to the AUC was then used to approximate the number of particles observed for the device with the centered through wire after the PZT was turned off for all durations of the acoustic wave presence. Noticeably, as the duration of the acoustic wave increased from 15 seconds to 2 minutes, there was an increase in trapped particles from 6800 particles to over 31 000 particles. The total number of trapped particles on the device with the centered through-wire was estimated between 52–91% of available particles to trap, isolating a significant portion of particles in the stream. Although total trapping efficiency does not achieve 100%, these studies demonstrate that greater than 50% of particles are trapped along the through-wire, while we can visually confirm a majority of the free particles are driven to the wire and continue to flow along the centered wire structure.

Referring to the COMSOL-generated velocity profiles (Fig. 3), the centered through-wire configuration exhibited the lowest maximum flow velocity ($\sim$5.5 mm s^{-1}), followed by the no-wire device ($\sim$7 mm s^{-1}), while the offset-wire configuration produced the highest velocity ($\sim$7.5 mm s^{-1}). These trends agree with classical concentric and eccentric flow behavior, where centrally positioned obstructions create uniform constriction and greater hydraulic resistance, whereas off-center obstructions generate an asymmetric channel. In the eccentric case, a wider flow gap forms on one side of the wire, resulting in a high-velocity bypass region that supports greater volumetric flow compared to both the concentric configuration and even the unobstructed channel.[56] COMSOL model showed that the off-center wire achieves a much slower flow velocity profile over a greater area around the wire (Fig. 3i) compared to the centered wire (Fig. 3h), arguing that particles would see a greater localized hydrodynamic residence time with the off-center wire. Even though particles are experiencing a greater localized hydrodynamic residence time with the off-center wire, the device with the center wire exhibits greater trapping efficiency. Although other work has demonstrated the successful capture and entrapment of particles using secondary forces, the positioning of the trapping medium was non-specifically placed.[26,28,29] The results demonstrated in this study highlight that the presence and positioning of the wire drives the acoustic trapping efficiency of particles within the capillary.

The objective of this study was to evaluate how introducing an axially positioned micron-sized wire into a resonating acoustofluidic channel influences particle trapping behavior. While the approach demonstrates promising trapping capability, several limitations should be acknowledged. As the acoustic wave exposure time increases, the heating of the PZT transducer is unavoidable, potentially influencing the particle behavior and entrapment mainly due to the variation in the applied frequency. This would then cause heat transfer from the PZT into the glass capillary, and ultimately the solution flowing through the microcapillary. As the temperature of the solution changes, the speed of sound within the solution also varies, leading to slight differences in the true resonant frequency of the system.[48] Infrared thermal measurements indicated that the capillary system temperature increased by only a few degrees Celsius during operation, as shown in Fig. S6. Over this temperature range the speed of sound in water varies by less than $\sim$1%, indicating that temperature-induced shifts in acoustic wavelength or resonance conditions are negligible for the experiments reported. The relative lack of heating to the system is likely attributable to the fact that the PZT is freely suspended in air from a narrow capillary, allowing for excellent air circulation and minimal surface area for efficient heat transfer. Additionally, we routinely only

operated the system for a few minutes before shutting power off to the PZT, and repowered the PZT for each run. Although we did not correct the applied frequency to optimally drive the system under various solution temperatures, the results undoubtedly demonstrate the impact of microstructure positioning within an acoustic wave to efficiently drive and capture microparticles. The material chosen for the through-wire was 50 μm stainless-steel wire. Alternatively, other materials and wire dimensions could have been chosen to evaluate the impacts on focusing efficiency. With regards to particle isolation using secondary acoustic forces, previous work demonstrated silica seed particles exhibited improved particle capture compared to PS seed particles, attributing this improvement to the material density differences.[30,57] Flow rate presents an additional constraint for seed particle approach, since elevated velocities generate greater hydrodynamic drag that can disrupt seed particle retention. Designing a trapping structure that experiences no fluid-induced disturbance would improve capture efficiency and overall stability. It is likely that differences in acoustic trapping would be seen if the material of the through-wire changed, as differences in acoustic impedance would be another potential driver for particle adherence. While the present work focuses on acoustic trapping of particles to a micro-scale structural feature within the capillary, this concentration mechanism may also support particle separation based on size. In acoustophoretic systems, the magnitude of the primary acoustic radiation force scales with particle volume, and particles of different sizes or acoustic contrast factors may therefore experience different trapping efficiencies or residence times near the microstructure. In this context, the wire-based trapping region could act as a localized concentration site from which particles of different sizes may be preferentially retained or released depending on the operating conditions. Although the present study demonstrates trapping using a single particle population, future work will explore the behavior of mixed particle populations and the potential for size-selective particle separation using this trapping geometry.

Conclusions

We have shown that precise positioning of microstructures axial to flow within acoustic waves leads to optimal acoustic trapping *via* secondary acoustic forces. This study expands upon previous work of microparticle enrichment using primary and secondary acoustic forces, and demonstrates the successful approach of our unique design to successfully entrap microparticles in a cylindrical capillary. Future work aims to evaluate the temperature dependencies of acoustic focusing in the presence of the stainless-steel through-wire, as well as acoustically trapping smaller particles, such as nanoparticles and biological samples, including cells and extracellular vesicles. Overall, this study lays the foundation for work focused on the design of optimally placed microstructures in laminar flow systems to optimize microparticle and nanoparticle trapping. This work demonstrates the proof-of-concept that placing small microstructures at the pressure node of an acoustic field does not hinder particle focusing and entrapment, but rather enhances particle trapping efficiency, and is therefore a novel approach for the future of acoustophoretic enrichment techniques.

Author contributions

Conceptualization: R. J. T., A. P. S., M. E. P., M. J. C. and S. W. G. Methodology: R. J. T., A. P. S., M. E. P., M. J. C. and S. W. G. Investigation: R. J. T. and P. H. B. Formal analysis: R. J. T., P. H. B., A. P. S., M. E. P., M. J. C. and S. W. G. Software/modeling (COMSOL): S. W. G. Data curation: R. J. T. and P. H. B. Writing – original draft: R. J. T. and S. W. G. Writing – review & editing: R. J. T., P. H. B., A. P. S., M. E. P., M. J. C. and S. W. G. Supervision: M. E. P. and S. W. G. All authors have read and approved the final manuscript.

Conflicts of interest

The authors do not have any conflicts of interest.

Data availability

The supporting data has been provided as part of the supplementary information (SI). Intensity data for Gaussian fits, raw pixel intensity sums, and MATLAB files used for data analysis are available at Harvard Dataverse at https://doi.org/10.7910/DVN/L6VSZT.

Supplementary information is available. See DOI: https://doi.org/10.1039/d6lc00047a.

Acknowledgements

Research reported in this publication was supported by the National Institute of Environmental Health Sciences of the National Institutes of Health under award number R21ES037164. Research reported in this publication was supported by UNM Rainforest Innovations, the UNM ARID Institute, and the Wellborn Gap Fund Award. We would like to acknowledge the UNM Center for Metals in Biology and Medicine – GM130422. We would like to acknowledge the technical help and expertise from Dr. John T. King in the Department of Chemical and Biological Engineering at the University of New Mexico. We would also like to acknowledge Nipuni de Silva and Dhanika Senavirathna from New Mexico Institute of Mining and Technology for their collaborative efforts.

References

1 R. Geyer, J. R. Jambeck and K. L. Law, *Sci. Adv.*, 2017, **3**, 1–5.
2 S. Moon, L. M. A. Martin, S. Kim, Q. Zhang, R. Zhang, W. Xu and T. Luo, *Sci. Adv.*, 2024, **10**, 1–8.

3 C. Schmidt, T. Krauth and S. Wagner, *Environ. Sci. Technol.*, 2017, **51**, 12246–12253.
4 L. Peng, D. Fu, H. Qi, C. Q. Lan, H. Yu and C. Ge, *Sci. Total Environ.*, 2020, **698**, 134254.
5 M. B. Paul, V. Stock, J. Cara-Carmona, E. Lisicki, S. Shopova, V. Fessard, A. Braeuning, H. Sieg and L. Böhmert, *Nanoscale Adv.*, 2020, **2**, 4350–4367.
6 A. J. Nihart, M. A. Garcia, E. E. Hayek, R. Liu, M. Olewine, J. D. Kingston, E. F. Castillo, R. R. Gullapalli, T. Howard, B. Bleske, J. Scott, J. Gonzalez-Estrella, J. M. Gross, M. Spilde, N. L. Adolphi, D. F. Gallego, H. S. Jarrell, G. Dvorscak, M. E. Zuluaga-Ruiz, A. B. West and M. J. Campen, *Nat. Med.*, 2025, **31**, 1114–1119.
7 H. A. Leslie, M. J. M. van Velzen, S. H. Brandsma, A. D. Vethaak, J. J. Garcia-Vallejo and M. H. Lamoree, *Environ. Int.*, 2022, **163**, 1–8.
8 S. Liu, C. Wang, Y. Yang, Z. Du, L. Li, M. Zhang, S. Ni, Z. Yue, K. Yang, Y. Wang, X. Li, Y. Yang, Y. Qin, J. Li, Y. Yang and M. Zhang, *J. Hazard. Mater.*, 2024, **469**, 1–7.
9 R. Marfella, F. Prattichizzo, C. Sardu, G. Fulgenzi, L. Graciotti, T. Spadoni, N. D'Onofrio, L. Scisciola, R. L. Grotta, C. Frigé, V. Pellegrini, M. Municinò, M. Siniscalchi, F. Spinetti, G. Vigliotti, C. Vecchione, A. Carrizzo, G. Accarino, A. Squillante, G. Spaziano, D. Mirra, R. Esposito, S. Altieri, G. Falco, A. Fenti, S. Galoppo, S. Canzano, F. C. Sasso, G. Matacchione, F. Olivieri, F. Ferraraccio, I. Panarese, P. Paolisso, E. Barbato, C. Lubritto, M. L. Balestrieri, C. Mauro, A. E. Caballero, S. Rajagopalan, A. Ceriello, B. D'Agostino, P. Iovino and G. Paolisso, *N. Engl. J. Med.*, 2024, **390**, 900–910.
10 M. A. Garcia, R. Liu, A. Nihart, E. E. Hayek, E. Castillo, E. R. Barrozo, M. A. Suter, B. Bleske, J. Scott, K. Forsythe, J. Gonzalez-Estrella, K. M. Aagaard and M. J. Campen, *Toxicol. Sci.*, 2024, **199**, 81–88.
11 L. Zhu, Y. Kang, M. Ma, Z. Wu, L. Zhang, R. Hu, Q. Xu, J. Zhu, X. Gu and L. An, *Sci. Total Environ.*, 2024, **915**, 170004.
12 A. Ragusa, A. Svelato, C. Santacroce, P. Catalano, V. Notarstefano, O. Carnevali, F. Papa, M. C. A. Rongioletti, F. Baiocco, S. Draghi, E. D'Amore, D. Rinaldo, M. Matta and E. Giorgini, *Environ. Int.*, 2021, **146**, 106274.
13 Y. Li, L. Tao, Q. Wang, F. Wang, G. Li and M. Song, *Environ. Health*, 2023, **1**, 249–257.
14 N. Chartres, C. B. Cooper, G. Bland, K. E. Pelch, S. A. Gandhi, A. BakenRa and T. J. Woodruff, *Environ. Sci. Technol.*, 2024, **58**, 22843–22864.
15 Q. Zhang, D. K. Jeppesen, J. N. Higginbotham, J. L. Franklin and R. J. Coffey, *Nat. Protoc.*, 2023, **18**, 1462–1487.
16 J. B. Miller, J. M. Harris and E. K. Hobbie, *Langmuir*, 2014, **30**, 7936–7946.
17 V. J. Pansare, D. Tien, P. Thoniyot and R. K. Prud'homme, *J. Membr. Sci.*, 2017, **538**, 41–49.
18 H. Guo, X. Li, W. Yang, Z. Yao, Y. Mei, L. E. Peng, Z. Yang, S. Shao and C. Y. Tang, *Front. Chem. Sci. Eng.*, 2022, **16**, 681–698.
19 W. M. Samhaber and M. T. Nguyen, *Beilstein J. Nanotechnol.*, 2014, **5**, 476–484.
20 H. Cai, M. Chen, F. Du, S. Matthews and H. Shi, *Water Res.*, 2021, **203**, 1–10.
21 Y. Xu, Q. Ou, X. Wang, J. P. van der Hoek and G. Liu, *ACS ES&T Water*, 2024, **4**, 3348–3358.
22 I. Chaïb, P. Doyen, P. Merveillie, A. Dehaut and G. Duflos, *J. Food Compos. Anal.*, 2025, **144**, 1–11.
23 M. Groschl, *Acustica*, 1998, **84**, 432–447.
24 T. Laurell, F. Petersson and A. Nilsson, *Chem. Soc. Rev.*, 2007, **36**, 492–506.
25 G. Goddard and G. Kaduchak, *J. Acoust. Soc. Am.*, 2005, **117**, 3440–3447.
26 B. Hammarström, T. Laurell and J. Nilsson, *Lab Chip*, 2012, **12**, 4296–4304.
27 T. Lilliehorn, U. Simu, M. Nilsson, M. Almqvist, T. Stepinski, T. Laurell, J. Nilsson and S. Johansson, *Ultrasonics*, 2005, **43**, 293–303.
28 S. Gupta and D. L. Feke, *Ultrasonics*, 1997, **35**, 131–139.
29 S. Gupta and D. L. Feke, *AIChE J.*, 1998, **44**, 1005–1014.
30 M. Havers, T. Baasch, A. Lenshof, M. Evander and T. Laurell, *Phys. Rev. Appl.*, 2024, **21**, 1–16.
31 A. Ku, J. Fredsøe, K. D. Sørensen, M. Borre, M. Evander, T. Laurell, H. Lilja and Y. Ceder, *Front. Oncol.*, 2021, **11**, 1–13.
32 A. Broman, A. Lenshof, M. Evander, L. Happonen, A. Ku, J. Malmstrom and T. Laurell, *Anal. Chem.*, 2021, **93**, 3929–3937.
33 R. Habibi and A. Neild, *Lab Chip*, 2019, **19**, 3032–3044.
34 R. Habibi, V. He, S. Ghavamian, A. D. Marco, T. H. Lee, M. I. Aguilar, D. Zhu, R. Lim and A. Neild, *Lab Chip*, 2020, **20**, 3633–3643.
35 L. N. Perera and M. E. Piyasena, *Sep. Purif. Technol.*, 2022, **288**, 1.
36 L. E. Kinsler, A. R. Frey, A. B. Coppens and J. V. Sanders, *Fundamentals of Acoustics*, 4th edn, 2000.
37 A. Habib, A. Shelke, M. Vogel, U. Pietsch, X. Jiang and T. Kundu, *Ultrasonics*, 2012, **52**, 989–995.
38 Z. Gibson, J. R. Dennison, L. Pearson, E. Griffiths, A. Pearson and V. Griseri, in *Conference Proceedings Materials Physics*, 2018.
39 W. P. Instruments, https://www.wpiinc.com/glass-capillaries, 2025.
40 COMSOL AB, *COMSOL Multiphysics® Material Library, Version 6.4. COMSOL Multiphysics® Reference Manual*, COMSOL AB, Stockholm, Sweden, 2025.
41 W. Marczak, *J. Acoust. Soc. Am.*, 1997, **102**, 2776–2779.
42 D. R. Lide, G. Baysinger, L. I. Berger, R. N. Goldberg, H. V. Kehiaian, K. Kuchitsu, D. L. Roth and D. Zwillinger, *CRC Handbook of Chemistry and Physics, Internet Version*, CRC Press, 2005.
43 G. Goddard, J. C. Martin, S. W. Graves and G. Kaduchak, *Cytometry, Part A*, 2006, **69**, 66–74.
44 G. R. Goddard, C. K. Sanders, J. C. Martin, G. Kaduchak and S. W. Graves, *Anal. Chem.*, 2007, **79**, 8740–8746.
45 M. D. Ward and G. Kaduchak, *Curr. Protoc. Cytom.*, 2018, **84**, 5–19.
46 M. T. Grossner, D. L. Feke and J. M. Belovich, *AIChE J.*, 2005, **51**, 1590–1598.

47 A. Barrio-Zhang, S. Anandan, A. Deolia, R. Wagner, D. M. Warsinger and A. M. Ardekani, *Sep. Purif. Technol.*, 2024, **342**, 1–10.
48 D. M. Kalb, R. J. Olson, H. M. Sosik, T. A. Woods and S. W. Graves, *PLoS One*, 2018, **13**, 1–20.
49 A. D. Pierce, *Acoustics: an introduction to its physical principles and applications*, McGraw-Hill Book Co., 1981.
50 D. Saeidi, M. Saghafian, S. H. Javanmard and M. Wiklund, *Micromachines*, 2020, **11**, 1–13.
51 G. Simon, M. A. B. Andrade, M. P. Y. Desmulliez, M. O. Riehle and A. L. Bernassau, *Micromachines*, 2019, **10**, 1–18.
52 M. Settnes and H. Bruus, *Phys. Rev. E: Stat., Nonlinear, Soft Matter Phys.*, 2012, **85**, DOI: 10.1103/PhysRevE.85.016327.
53 G. T. Silva and H. Bruus, *Phys. Rev. E: Stat., Nonlinear, Soft Matter Phys.*, 2014, **90**, DOI: 10.1103/PhysRevE.90.063007.
54 R. E. Apfel, *Am. J. Phys.*, 1988, **56**, 726–729.
55 M. A. Weiser, R. E. Apfel and E. A. Neppiras, *Acta Acust. Acust.*, 1984, **56**, 114–119.
56 R. Alassar, *J. Fluids Eng.*, 2017, **139**, DOI: 10.1115/1.4035115.
57 M. Evander, O. Gidlöf, B. Olde, D. Erlinge and T. Laurell, *Lab Chip*, 2015, **15**, 2588–2596.

